

Dual-Input Dynamic Convolution for Positron Range Correction in PET Image Reconstruction

Youness Mellak, Alexandre Bousse, Thibaut Merlin, Élise Émond, Dimitris Visvikis

Abstract—Positron range (PR) blurring degrades positron emission tomography (PET) image resolution, particularly for high-energy emitters like gallium-68 (^{68}Ga). We introduce Dual-input Dynamic Convolution (DDConv), a novel computationally efficient approach trained with voxel-specific PR *point spread functions* (PSFs) from Monte Carlo (MC) simulations and designed to be utilized within an iterative reconstruction algorithm to perform PR correction (PRC). By dynamically inferring local blurring kernels through a trained convolutional neural network (CNN), DDConv captures complex tissue interfaces more accurately than prior methods. Crucially, it also computes the transpose of the PR operator, ensuring consistency within iterative PET reconstruction. Comparisons with a state-of-the-art, tissue-dependent correction confirm the advantages of DDConv in recovering higher-resolution details in heterogeneous regions, including bone-soft tissue and lung-soft tissue boundaries. Experiments across digital phantoms, MC-simulated data, and patient scans verify that DDConv remains clinically practical through GPU-accelerated convolutions, offering near-MC accuracy while significantly reducing computation times. These results underline DDConv’s potential as a routine tool in PET imaging, improving both resolution and fidelity without placing excessive demands on reconstruction resources.

Index Terms—PET, Positron Range (PR), Monte-Carlo (MC) Simulations, Deep Learning.

I. INTRODUCTION

Positron emission tomography (PET) is a nuclear imaging technique that visualizes molecular and metabolic processes by detecting pairs of gamma photons emitted during positron-electron annihilation. During a PET scan, a radiopharmaceutical—a biologically active molecule labeled with a positron-emitting radionuclide—is administered to the patient. As the radionuclide decays, it emits positrons, which travel a short distance through tissue before annihilating with electrons. This distance, also referred to as positron range (PR), displaces the annihilation site from the original tracer location, introducing an inherent blur into the reconstructed image. The PR is governed by two factors: the radionuclide’s positron endpoint energy (the maximum kinetic energy of emitted positrons) and the electron density of the surrounding tissue (e.g., dense bone attenuates positrons more effectively than low-density lung tissue). For widely used radionuclides such as fluorine-18 (^{18}F) which has a low endpoint energy (0.634 MeV), the PR is minimal (0.6 mm in water). This

blur is negligible compared to the 2–4 mm spatial resolution of modern PET scanners, enabling precise imaging of glucose metabolism in oncology. However, clinical demands increasingly require isotopes with higher positron energies. Gallium-68 (^{68}Ga), used for prostate cancer imaging, exhibits a 1.9 MeV endpoint energy and a PR of 2.9 mm in water. Similarly, rubidium-82 (^{82}Rb), employed in cardiac perfusion studies, has a 3.4 MeV endpoint energy and a PR of 5.9 mm. These PR values exceed the resolution of the scanner, leading to significant blurring that distorts quantitative metrics such as lesion size and standardized uptake values. This problem is amplified in heterogeneous tissues (e.g., tumor-lung interfaces), where abrupt changes in electron density further widen the PR distribution.

Various PR correction (PRC) methods have been developed to mitigate blurring effects caused by PR in PET imaging, particularly for radionuclides such as ^{68}Ga [1]. These methods can be broadly categorized into four approaches.

The first involves reducing the travel distance of the positron by applying strong magnetic fields to confine its trajectory [2], [3]. While effective, this method requires extremely intense magnetic fields, making it expensive and challenging to implement in clinical PET scanners.

The second approach consists in applying PRC before reconstruction (pre-reconstruction) using deconvolution techniques on measured projections [4], [5]. Although effective in homogeneous regions, this method assumes a uniform blurring profile, limiting its accuracy in heterogeneous tissues where spatially varying PR effects are significant.

The third approach applies corrections directly to reconstructed PET images, offering a practical solution when incorporating corrections during acquisition or reconstruction is not feasible. For example, Deep-PRC [6], [7] uses convolutional neural network (CNN) to map ^{68}Ga -blurred images to ^{18}F -like images which was trained on images reconstructed from Monte Carlo (MC)-simulated data, effectively reducing blurring. However, this method is highly dependent on the quality of the training data, reconstruction parameters, and detected counts. Furthermore, self-supervised models have been proposed [8], simulating ^{82}Rb PR kernels using MC methods and employing pseudo-labels from ^{18}F -fluorodesoxyglucose images to approximate the inverse kernel. While promising, these models are limited to homogeneous kernels, restricting their applicability in heterogeneous tissues.

The fourth approach integrates PRC directly into the iterative reconstruction process by modeling spatially-variant PR effects in the forward model using voxel-specific convolution kernels. High-precision methods derived from MC simulations

This work did not involve human subjects or animals in its research.

Y. Mellak, A. Bousse, T. Merlin and D. Visvikis are with Univ. Brest, LaTIM, Inserm, U1101, 29238 Brest, France.

É. Émond is with Brainlab, Munich, Germany.

Corresponding authors: bousse@univ-brest.fr

with tissue-specific kernels achieve accurate PR blurring, but they do not incorporate PR in the transpose model and remain computationally expensive [9], even with generative adversarial network (GAN)-based acceleration [10]. Various kernel-based approaches have been developed to address the computational and accuracy challenges of PRC. Cal-Gonzalez *et al.* [11] introduced tissue-dependent and spatially variant kernels derived from MC simulations. However, the computational intensity of MC simulations limits their clinical practicality. Bertolli *et al.* [12] proposed isotropic and material-specific kernels as a computationally efficient alternative. Although efficient, this approach struggles to accurately capture PR effects at complex tissue interfaces. Kraus *et al.* [13] addressed the challenge of PR blurring in heterogeneous environments by precomputing tissue-specific kernels, such as those for lung-soft tissue boundaries. This method improved spatial resolution and reduced artifacts, but lacked adaptability to finer-scale variations within tissues. Kertész *et al.* [14] refined this approach by dynamically combining precomputed homogeneous kernels based on attenuation maps. This allowed for better adaptability in complex anatomies but introduced trade-offs in precision, as the composition of kernels could still deviate from the true spatial distribution of PR blurring, especially near tissue interfaces. In addition to kernel-based techniques, deep learning methods have emerged as a promising alternative. Merlin *et al.* [15] proposed an image translation GAN integrated into an expectation maximization (EM) reconstruction framework to dynamically correct PR effects during forward projection. This approach demonstrated improved contrast recovery, particularly in low-attenuation tissues, although it operates with an unmatched projector. In contrast, Mellak *et al.* [16] introduced a graph neural network-based method that locally predicts the weights of the linear operator responsible for PR blurring. This design inherently allows for straightforward computation of the transpose, making it seamlessly integrated during iterative reconstruction algorithms.

In this study, we expand on previous work and propose a novel method for PRC, namely Dual-input Dynamic Convolution (DDConv), which can be plugged into iterative PET image reconstruction, leveraging a dynamic CNN to address accuracy and computational time. Our method is trained on MC-simulated data using the Geant4 Application for Tomography Emission (GATE) [17] in order to accurately model PR blurring while significantly reducing computational demands. The method inherently computes the transpose of the blurring operator, ensuring consistency between forward and backward projections within iterative reconstruction algorithms.

Section II provides a background on PR in PET iterative reconstruction, and present DDConv, including the forward blurring and its transposed version, as well as the MC-trained PR *point spread function* (PSF) predictor. Section III compares DDConv with a state-of-the-art method from the literature, the spatially-variant and tissue-dependent (SVTD) PRC method by Kertész *et al.* [14]. The results of this research are summarized in Section IV and Section IV concludes this paper. A method to reduce DDConv computational time is proposed in the Appendix.

Nomenclature

In the following, ‘ \top ’ denotes the matrix transposition. For a given a real-valued matrix $\mathbf{A} = \{a_{n,m}\}_{n,m=1}^{N,M} \in \mathbb{R}^{N \times M}$, $[\mathbf{A}]_{n \times m}$ refers to the entry at position (n, m) in \mathbf{A} , i.e., $[\mathbf{A}]_{n,m} = a_{n,m}$.

The three-dimensional (3-D) image is composed of J voxels listed in the set $\mathcal{S} = \{1, \dots, J\}$. An image defined on \mathcal{S} takes the form of a real-valued column vector $\mathbf{x} = [x_1, \dots, x_J]^\top \in \mathbb{R}^J$ such that for all j the value x_j is the image intensity at voxel j . Given a subset of voxels $\mathcal{T} \subset \mathcal{S}$, $\mathbf{x}_{\mathcal{T}}$ denotes the restriction of \mathbf{x} to \mathcal{T} , i.e., $\mathbf{x}_{\mathcal{T}} = \{x_j\}_{j \in \mathcal{T}} \subset \mathbb{R}^m$, with $m = \text{card}(\mathcal{T})$.

For all voxel j , \mathcal{N}_j denotes the closed neighborhood of j , i.e., $k \in \mathcal{N}_j \Leftrightarrow j \in \mathcal{N}_k$ for all (j, k) and $j \in \mathcal{N}_j$ for all j . In this work, we defined \mathcal{N}_j as the $11 \times 11 \times 11$ box centered on j for all $j = 1, \dots, J$ (omitting boundary constraints), and we define by $m = \text{card}(\mathcal{N}_j) = 11^3$ the number of voxels in each neighborhood. This box covers the maximum PR for 2-mm cubic voxels.

$\mathbf{0}$ and $\mathbf{1}$ respectively denote the zero vector and the vector consisting entirely of ones, with dimensions determined by the context.

II. MATERIALS AND METHODS

A. Problem Formulation

The objective of PET reconstruction is to retrieve an activity image $\mathbf{x} = [x_1, \dots, x_J]^\top \in \mathbb{R}^J$ from a measurement $\mathbf{y} = [y_1, \dots, y_I]^\top \in \mathbb{R}^I$, I being the number of detector pairs in the PET system, by matching the expected measurement $\bar{\mathbf{y}}(\mathbf{x}) = [\bar{y}_1(\mathbf{x}), \dots, \bar{y}_I(\mathbf{x})]^\top \in \mathbb{R}^I$, given by the linear relation

$$\bar{\mathbf{y}}(\mathbf{x}) = \mathbf{H}\mathbf{x} + \mathbf{r} \quad (1)$$

where $\mathbf{H} \in \mathbb{R}^{I \times J}$ represents the PET system matrix, such that $[\mathbf{H}]_{i,j}$ denotes the probability that an emission originating from voxel j leads to an annihilation event producing a pair of γ -photons detected by detector pair i , and $\mathbf{r} \in \mathbb{R}^I$ is a background vector representing expected scatter and randoms. The reconstruction is performed via an optimization problem of the form

$$\min_{\mathbf{x}} \ell(\mathbf{y}, \bar{\mathbf{y}}(\mathbf{x})) \quad (2)$$

where ℓ is a loss function that evaluates the goodness of the fit between \mathbf{y} and $\bar{\mathbf{y}}(\mathbf{x})$, generally defined as the negative Poisson log-likelihood, i.e., $\ell(\mathbf{y}, \bar{\mathbf{y}}) = \sum_i -y_i \log \bar{y}_i - \bar{y}_i$, in which case solving (2) is achieved via an EM algorithm [18] which computes the estimate $\mathbf{x}^{(q+1)}$ at iteration $q+1$ from the estimate $\mathbf{x}^{(q)}$ at iteration q with the updating rule

$$\mathbf{x}^{(q+1)} = \frac{\mathbf{x}^{(q)}}{\mathbf{H}^\top \mathbf{1}} \mathbf{H}^\top \left(\frac{\mathbf{y}}{\mathbf{H}\mathbf{x}^{(q)} + \mathbf{r}} \right). \quad (3)$$

where all vector operations are to be understood element-wise.

The PET system matrix \mathbf{H} depends on the system’s geometry, the linear attenuation 3-D image $\boldsymbol{\mu} \in \mathbb{R}^J$ —usually derived from an anatomical image such as computed tomography (CT) or magnetic resonance (MR)—and PR which depends on the 3-D electronic density image $\boldsymbol{\rho} \in \mathbb{R}^J$. In the context of PET imaging, $\boldsymbol{\mu}$ and $\boldsymbol{\rho}$ are strongly correlated and therefore we

assume that PR is determined by μ . The matrix H can be decomposed as [19]

$$H = A(\mu)PB(\mu) \quad (4)$$

where $A(\mu) \in \mathbb{R}^{I \times I}$ is a diagonal matrix representing the attenuation factors along the lines of response (LORs) for each detector pair, $P \in \mathbb{R}^{I \times J}$ is the PET geometric projector defined such that $[P]_{i,j}$ is the probability that an annihilation taking place at voxel j is detected on i in absence of attenuation (taking into account sensitivity and detector resolution), and $B(\mu)$ is the PR blurring operator defined such that $[B(\mu)]_{j',j}$ is the probability that a positron emitted in j interacts with an electron in j' .

The geometric projector P is known from the system's manufacturer, while $A(\mu)$ can be computed by integrating μ along each LOR. The PR blurring operator $B(\mu)$ is more challenging, as it performs position-dependent blurring. Consequently, it is often replaced by the identity matrix or a position-independent blurring operator [4], which may underestimate PR in regions with low electron density, such as the lungs.

A CNN can be trained to approximate $B(\mu)x$ by taking x and μ as inputs and directly producing an image with PR blurring applied [15]. While computationally efficient, this approach projector P . Moreover, it cannot compute the transpose of the PR operator $B(\mu)^\top$, leading to the use of an unmatched forward model in the iterative scheme (3).

B. Dual-Input Dynamic Convolution for Positron Range Modeling

This section describes our DDConv implementation of the PR blurring $x \mapsto B(\mu)x$ and its transposed version $z \mapsto B(\mu)^\top z$ which are involved in the EM algorithm (3) though H and H^\top .

1) *Matrix Formulation*: The blurring operator $B(\mu) \in \mathbb{R}^{J \times J}$ models the PR-induced spatial blurring, transforming an activity distribution image $x \in \mathbb{R}^J$ into an annihilation distribution image $z = [z_1, \dots, z_J]^\top \in \mathbb{R}^J$ defined as

$$z = B(\mu)x, \quad (5)$$

which represents the spatial locations where positrons undergo annihilation. The attenuation map μ governs this process by defining the local electron density and tissue composition, which influence positron propagation before annihilation. In the following, we assume that PR is bounded. More precisely, we assume that a positron emission at voxel j results in an annihilation in a $11 \times 11 \times 11$ closed neighborhood of j , denoted \mathcal{N}_j , and we define $m \triangleq \text{card}(\mathcal{N}_j) = 11^3$.

For all $j = 1, \dots, J$, the probability that a positron emitted from j annihilates with an electron located in voxel $k \in \mathcal{N}_j$ is denoted $w_{j \rightarrow k} \in [0, 1]$ and is entirely determined by $\mu_{\mathcal{N}_j} \in \mathbb{R}^m$ for a given radiotracer, and we assume that annihilation is certain, i.e.,

$$\sum_{k \in \mathcal{N}_j} w_{j \rightarrow k} = 1. \quad (6)$$

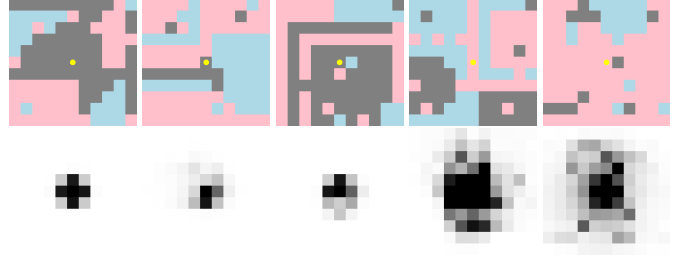


Fig. 1: Random material images η (upper row) with tissue-specific color coding—pink for lung, light blue for water, and gray for bone—and their corresponding MC-generated PR PSF w_η (annihilation image). The yellow spot represents the ^{68}Ga positron-emitting point source.

In other words, the vector $w_j = \{w_{j \rightarrow k}\}_{k \in \mathcal{N}_j} \in \mathbb{R}^m$ is the PSF at pixel j . The annihilation distribution image z is obtained at each voxel k by performing a sum of the activity values of $x_{\mathcal{N}_k}$ weighted by the $w_{j \rightarrow k}$'s, $j \in \mathcal{N}_k$,

$$z_k = \sum_{j \in \mathcal{N}_k} w_{j \rightarrow k} \cdot x_j \quad (7)$$

and thus we have defined blurring operator $B(\mu)$ as

$$[B(\mu)]_{k,j} = \begin{cases} w_{j \rightarrow k} & \text{if } j \in \mathcal{N}_k, \\ 0 & \text{otherwise.} \end{cases} \quad (8)$$

2) *PR Prediction using a CNN*: The position-dependent PSF $\{w_j\}_{j \in S}$ cannot be stored and therefore we opted for an on-the-fly implementation of the blurring operator $B(\mu)$.

We used a CNN $G_\theta: \mathbb{R}^m \times \mathbb{R}^m \rightarrow \mathbb{R}^m$ with trainable parameter θ to predict w_j from $\mu_{\mathcal{N}_j}$. Additionally, G_θ takes as input a constant vector $d = \{d_{j,k}\}_{k \in \mathcal{N}_j}$ with $d_{j,k} = \text{dist}(j,k)$ to provide spatial information to the CNN—this process has been used by Hu *et al.* [20]. Training of G_θ is performed using small random N -material $11 \times 11 \times 11$ images $\eta \in \{1, 2, \dots, N\}^m$ ($m = 11^3$), such that $[\eta]_j = n$ if and only if voxel j is located in the n -th material (without material overlap). In this work, we considered the lung, rib bone and water materials ($N = 3$). For each material image η , a MC simulation is performed using GATE [17] with a ^{68}Ga positron-emitting point source at the center of η to generate a PSF $w_\eta \in \mathbb{R}^m$. We used 1 million positron emission events to generate a single PR PSF w_η . Figure 1 shows examples of material images η and their corresponding PR PSF w_η in a $11 \times 11 \times 11$ window with 2-mm cubic voxels.

Supervised training of the CNN G_θ is achieved by solving the optimization problem

$$\min_{\theta} \mathbb{E}_\eta [L(G_\theta(\mu_\eta, d), w_\eta)] \quad (9)$$

where $\mu_\eta \in \mathbb{R}^m$ is the attenuation map corresponding to η and L is a loss function. The complete architecture of G_θ is illustrated in Figure 2 (right). To compute (9), we employed an ℓ^1 loss function and generated 1,000 realizations of η .

3) *Implementation of the Blurring*: At each voxel j , the PSF w_j is computed from the local attenuation map $\mu_{\mathcal{N}_j}$ using G_θ to redistribute the activity value x_j in \mathcal{N}_j , using a spread operation defined as

$$\text{spread}(x_j, w_j) = \{w_{j \rightarrow k} \cdot x_j\}_{k \in \mathcal{N}_j} \quad (10)$$

In our implementation, this operation is achieved using the `torch.nn.ConvTranspose3d` module provided by PyTorch [21], [22]. Starting from an initial annihilation image $z = \mathbf{0}$, the final annihilation image is obtained by summing up the spread activity for each neighborhood \mathcal{N}_j :

$$z_{\mathcal{N}_j} \leftarrow z_{\mathcal{N}_j} + \text{spread}(x_j, w_j). \quad (11)$$

Conversely, the transposed blurring operator $B(\mu)^\top$ is performed at each voxel j by summing the annihilation image over \mathcal{N}_j with weights $w_{j \rightarrow k}$, i.e.,

$$x_j \leftarrow \sum_{k \in \mathcal{N}_j} w_{j \rightarrow k} \cdot z_k. \quad (12)$$

All these operations can be performed in parallel and in batches of voxels \mathcal{B}_q with $\mathcal{S} = \cup_{q=1}^Q \mathcal{B}_q$, $\mathcal{B}_q \cap \mathcal{B}_p = \emptyset$.

The overall DDConv methodology to compute $B(\mu)x$ and $B(\mu)^\top z$ is summarized in Figure 2, Algorithm 1 and Algorithm 2.

Algorithm 1 PR blurring

Require: x (activity), μ (attenuation map), G_θ (PSF predictor), $\mathcal{S} = \cup_{q=1}^Q \mathcal{B}_q$ with $\mathcal{B}_q \cap \mathcal{B}_p = \emptyset$ for all $q \neq p$ (batch decomposition).

- 1: $z \leftarrow \mathbf{0}$ ▷ initialization
 - 2: **for** $q = 1, \dots, Q$ **do**
 - 3: **for** $j \in \mathcal{B}_q$ **do**
 - 4: $w_j \leftarrow G_\theta(\mu_{\mathcal{N}_j}, d)$
 - 5: $z_{\mathcal{N}_j} \leftarrow z_{\mathcal{N}_j} + \text{spread}(x_j, w_j)$
 - 6: **end for**
 - 7: **end for**
 - 8: **return** z
-

Algorithm 2 PR transposed blurring

Require: z (annihilation image), μ (attenuation map), G_θ (PSF predictor), $\mathcal{S} = \cup_{q=1}^Q \mathcal{B}_q$ with $\mathcal{B}_q \cap \mathcal{B}_p = \emptyset$ for all $q \neq p$ (batch decomposition).

- 1: $x \leftarrow \mathbf{0}$ ▷ initialization
 - 2: **for** $q = 1, \dots, Q$ **do**
 - 3: **for** $j \in \mathcal{B}_q$ **do**
 - 4: $w_j \leftarrow G_\theta(\mu_{\mathcal{N}_j}, d)$
 - 5: $x_j \leftarrow \sum_{k \in \mathcal{N}_j} w_{j \rightarrow k} \cdot z_k$
 - 6: **end for**
 - 7: **end for**
 - 8: **return** x
-

III. EXPERIMENTS AND RESULTS

A. Experimental Setup and Dataset for Positron Range Correction Evaluation

The performance of the proposed method was benchmarked against the SVTD PRC method by Kertész *et al.* [14]. This approach utilizes a tissue-dependent anisotropic PSF. Instead of modeling fully spatially-variant kernels, the method approximates positron range effects by selecting and combining pre-calculated homogeneous MC-derived PSF's for different tissue types (e.g., lung, soft tissue, bone). Attenuation correction maps from attenuation images guide the spatial assignment, and voxel-specific kernels are estimated by weighting and normalizing contributions from adjacent tissue types to ensure smooth transitions and activity conservation across interfaces. All computations were accelerated using GPU parallelization with PyTorch, achieving substantial improvements in computational efficiency without compromising accuracy.

We first evaluated the accuracy of the PR blurring on digital phantoms (Experiment 1), then in image reconstruction on MC-simulated data (Experiment 2) and patient data (Experiment 3).

We used a $2 \times 2 \times 2$ -mm³ voxel size for all experiments.

For reconstruction, we used a Siemens mMR PET scanner, which has a 60-cm inner diameter, a 90-cm outer diameter, and lutetium oxyorthosilicate crystals measuring $4 \times 4 \times 20$ mm³. Image reconstructions were performed by EM using CASToR [23] with incorporation of DDConv (i.e., $B(\mu)$ and $B(\mu)^\top$).

We performed reconstruction from MC-simulated data from digital and Extended Cardiac-Torso (XCAT) phantoms as well as from patient data acquired at University Hospital Poitiers, Poitiers, France. Raw PET data were acquired with 200-ps time-of-flight (TOF) resolution for the simulated data (no TOF for patient data). The $4.4 \times 4.4 \times 4.4$ -mm³ full width at half maximum intrinsic resolution of the system was incorporated in P . No post-reconstruction filtering was applied.

B. Experiment 1: Blurring Accuracy

1) *Geometric Phantom*: To investigate the spatial variation of PR distributions in heterogeneous tissue environments, we designed a series of controlled digital phantoms that simulate distinct biological compositions relevant to PET imaging, following the approach of Kertész *et al.* [14]. Each phantom is represented as a 3-D volume of $62 \times 62 \times 62$ mm³, with a ⁶⁸Ga point source (initial activity = 10 MBq) placed at the center. We considered five distinct configurations (Figure 3): (i) a lung–water interface, where lung tissue occupies the anterior 26 mm along the z -axis, while the remaining 36 mm is filled with water; (ii) a lung background with a centrally embedded 12×12 mm² water inclusion spanning the full 62 mm in the x -dimension; (iii) a water matrix containing a 12×12 mm² lung region, offset by 4 mm along the y -axis. (iv) a water background embedding a 12×12 mm² lung inclusion that contains a 2-mm bone column extending along the entire x -dimension; (v) the same as (iv), except the lung inclusion is shifted an additional 2 mm (one voxel) along the y -axis, while the bone column remains fixed.

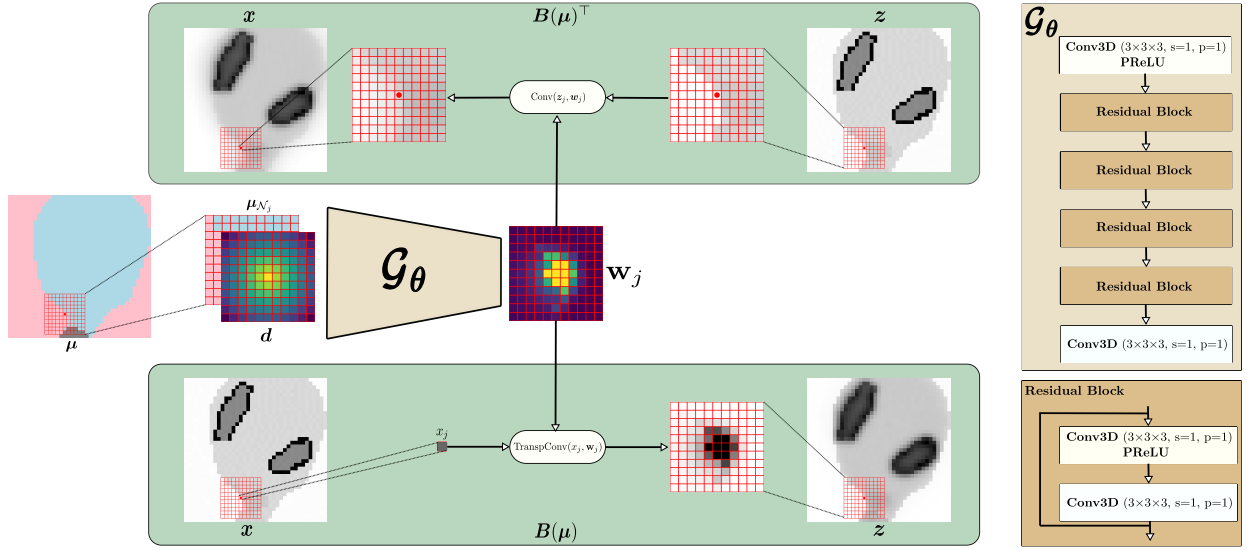


Fig. 2: Illustration of the PR blurring operators. The top section represents the transposed operator $B(\mu)^T$, while the bottom section shows the forward operator $B(\mu)$. Both operations use spatially varying PSFs w_j predicted by the same model G_θ , based on local attenuation μ_{N_j} . The right side details the architecture of G_θ .

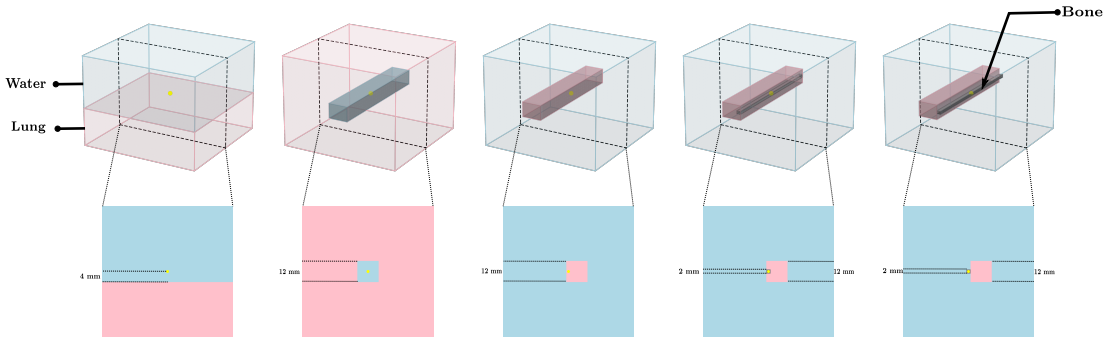


Fig. 3: Experiment 1—Digital phantoms used to assess PR blurring accuracy.

Figure 4 shows the results of the PR blurring from MC simulation (reference), SVTD and the proposed DDConv. The proposed method DDConv produces positron annihilation distributions that closely match those obtained from the reference GATE MC simulations across all phantom configurations, highlighting its accuracy in heterogeneous tissue environments. In contrast, the SVTD method exhibits significant deviations from the GATE distributions, indicating that it is less reliable for accurately modeling complex spatial variations in PR.

2) *XCAT Phantom*: We proceeded with a similar experiment but this time with an XCAT-generated ^{68}Ga activity distribution (Figure 5a) with the corresponding XCAT-generated material image (Figure 5b). The activity distribution contains four hot lesions: two in the lung, one at the interface between the lung and soft tissues, and one at the interface between the lung and the liver.

We observe that the blurring of Lesion 1 and Lesion 2 is accurately achieved by both SVTD and DDConv. However, SVTD fails to blur Lesion 3 and Lesion 4 accurately due to its inability to model PR in heterogeneous regions, whereas DDConv remains precise.

Analysis of the line profile further highlights these differences. SVTD exhibits moderate broadening due PR but shows reduced intensity in heterogeneous regions, indicating an underestimation of localized activity, while DDConv nearly coincides with the MC reference.

C. Experiment 2: Reconstruction from MC-simulated Data

Reconstruction was performed on MC-simulated data from the same phantom as in Section III-B2 (same tumor numbering) with 120 EM iterations on a $200 \times 200 \times 100$ voxel grid. ($2 \times 2 \times 2$ -mm³). Three strategies were compared: no PRC, SVTD and the proposed DDConv approach. Figure 6 shows the reconstructed images at different iterations. For tumors entirely located in homogeneous lung tissue (tumors 1 and 2), both SVTD and DDConv produced similar results. In contrast, tumor 4—located in heterogeneous tissues—was accurately reconstructed with DDConv, while SVTD failed to capture the lung component and the interface between the lung and the liver. These observations are validated by line profiles (Figure 7). For lesion 4, the reconstruction performance varies between water and lung regions. In the water region, the no-PRC reconstruction method recovers activity close to the

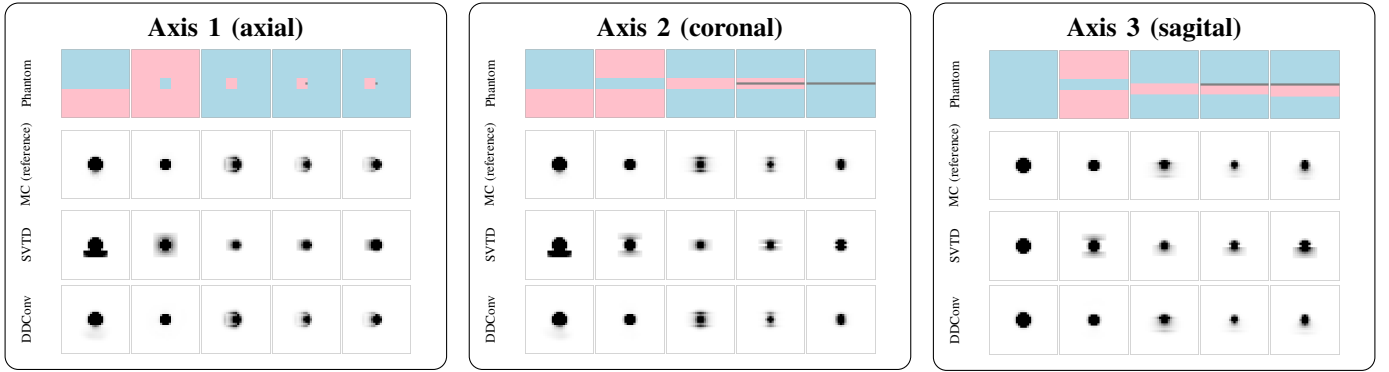


Fig. 4: Experiment 1—Overview of PR distributions across different viewing axes with the digital phantoms from Figure 3 with MC simulations (reference), SVTD and DDConv.

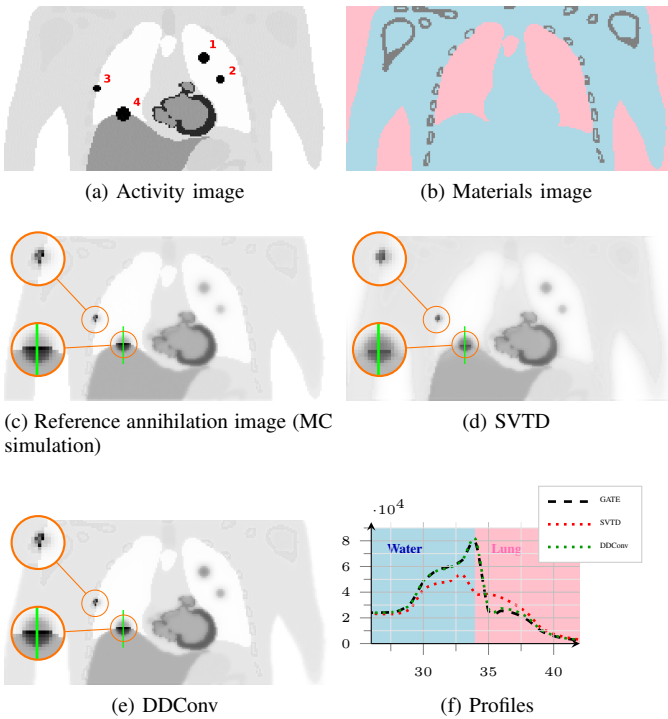


Fig. 5: Experiment 1—PR blurring experiment with the XCAT phantom: (a) activity phantom, (b) material phantom, (d) SVTD-blurred activity, (c) annihilation image (MC simulation), (e) DDConv-blurred activity and (f) profiles across the green line.

ground truth, whereas the SVTD method tends to over estimate the activity. In the lung region, both no-PRC and SVTD reconstructions exhibit loss of activity, failing to capture the true signal. In contrast, the DDConv reconstruction method consistently approximates the true activity in both regions, offering a stable recovery and a smoother transition at the interface between water and the lung.

D. Experiment 3: Reconstruction from Patient Data

We evaluated SVTD, DDConv and no-PRC reconstructions from a patient data set. The reconstructions were performed

with the same setting as in Section III-C except we used a $344 \times 344 \times 127$ voxel grid.

Figure 8 shows the reconstructed images at different iterations. The three reconstructions appear similar, however the line profile analysis (Figure 9) around the tumor shows that SVTD and DDConv recover more activity.

IV. DISCUSSION

A primary advantage of the proposed DDConv approach is its ability to generate PR blurring kernels with an accuracy similar to that of MC simulations. This strategy bridges a long-standing gap in PRC: it achieves rigorous physics-based modeling of annihilation distributions and can be readily incorporated into an EM algorithm while requiring only a few seconds to process an entire emission volume. Another critical feature is the forward-backward operator consistency inherent to the DDConv design. Unlike schemes that only incorporate forward PRC (i.e., in the forward projection), our approach guarantees the convergence of the EM algorithm. While the present PyTorch-based implementation is efficient, further accelerations could be achieved with a native CUDA implementation or using advanced GPU programming frameworks such as Triton [24].

Compared to prior PRC methods, DDConv offers substantial benefits in both precision and speed. Early approaches precomputed few generic kernels for different materials, or utilized simple deconvolutions; although computationally efficient, these approaches often fail at modeling PR at lung-soft tissue or bone-soft tissue interfaces. Recent anisotropic spatially-variant kernels improve accuracy but still rely on combining multiple precomputed kernels, sometimes introducing trade-offs in accuracy or speed. In contrast, DDConv spatially-variant PSF in real time for each voxel neighborhood, thus maintaining MC-like fidelity even in complex, inhomogeneous regions. The method's efficiency stems from its GPU-based convolutional design: the heavy computation of blurring is delegated to highly optimized parallel operations, enabling fast kernel estimation across large images without sacrificing the high fidelity needed for accurate quantification (cf. Appendix). Notably, the full computation of SVTD and DDConv for an entire XCAT phantom volume takes approximately 18 seconds, demonstrating that the proposed approach remains

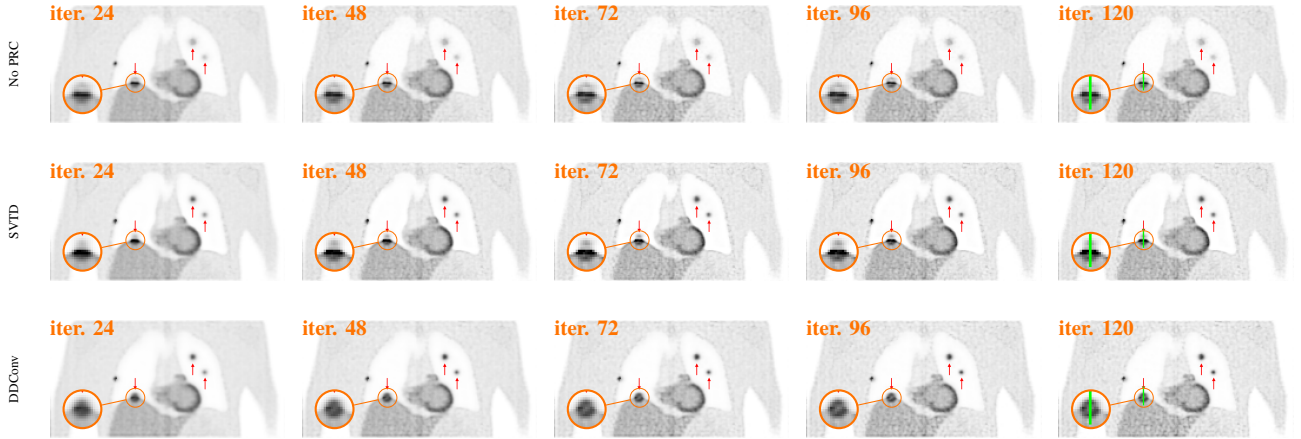


Fig. 6: Experiment 2—EM-reconstructed images (MC-simulated data) with no PRC, SVTD and DDConv at different iterations.

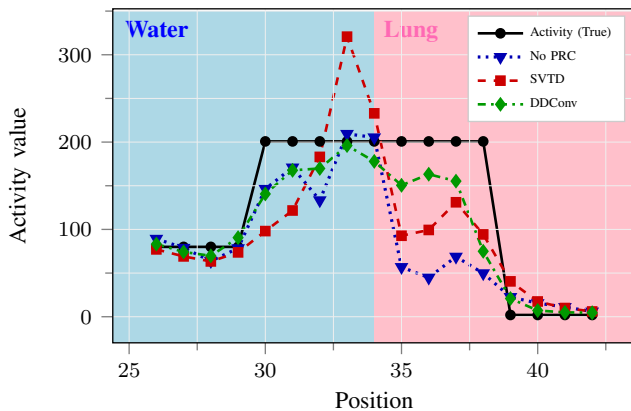


Fig. 7: Experiment 2—Line profiles of the reconstructed images (MC-simulated data, 120 EM iterations, cf. the green line in Figure 6) through tumor 4 with no PRC, SVTD and DDConv, at the interface between the water (light blue) and lung (soft pink) regions.

practical for clinical applications with graphics processing unit acceleration.

Our preliminary results on patient data indicate that DDConv performs on par with SVTD in homogeneous regions. Further experiments should be conducted on tumors located at the interface between different tissue types.

From a clinical perspective, achieving accurate PRC can significantly improve image resolution and lesion detectability, particularly for higher-energy tracers such as ^{68}Ga . The ability to correct for range-induced blurring in lung or bone interfaces offers more consistent quantitative accuracy across the field of view. By delivering sharper images and preserving quantitative consistency for a wide array of positron emitters, DDConv has the potential to improve PET imaging standards and expand the use of isotopes previously considered too susceptible to range effects.

V. CONCLUSION

In conclusion, this study introduced DDConv as an efficient and accurate framework for positron range correction in PET

imaging. By combining local attenuation maps with activity information, DDConv dynamically estimates high-resolution blurring kernels, matching MC accuracy at a fraction of the computational cost. Unlike previous methods that rely on precomputed or approximate models, DDConv’s predictive approach integrates seamlessly into iterative reconstruction and preserves consistency between forward and backward operations. Demonstrations on digital phantoms and patient data confirm its ability to improve image resolution and quantitative accuracy, especially for high-energy positron emitters. These results underscore the clinical potential of DDConv for routine PET, enabling near-MC-level corrections without prohibitive run times and thus contributing to more reliable disease detection and characterization.

APPENDIX

ACCELERATION

The computation of $B(\mu)x$ and $B(\mu)^\top z$ can be accelerated by considering a single PR PSF for homogeneous region on which the PSF is independent of the position.

A. Homogeneity map

We considered a decomposition of the $L = 3$ material (soft tissues, lungs and bones) which provides the binary images $\mathbf{u}_l \in \{0, 1\}^J$, $l = 1, \dots, L$, such that $\sum_{l=1}^L \mathbf{u}_l = \mathbf{1}$. For each material l , a single PR PSF, which takes the form of an $11 \times 11 \times 11$ image $\mathbf{h}_l \in \mathbb{R}^m$ ($m = 11^3$), is generated from MC simulations using a positron emission source in an homogeneous attenuation medium corresponding; each of these PSF is an isotropic Gaussian function. For each region l , the blurred material images are computed, i.e.,

$$\mathbf{v}_l = \mathbf{u}_l * \mathbf{h}_l \quad (13)$$

where ‘*’ denotes the standard convolution with a position-independent kernel. Each image \mathbf{v}_l ranges in $[0, 1]$ and we define the subsets of indices

$$\mathcal{S}_{\text{hom}}^l = \{j \in \mathcal{S}, [\mathbf{v}_l]_j = 1\}. \quad (14)$$

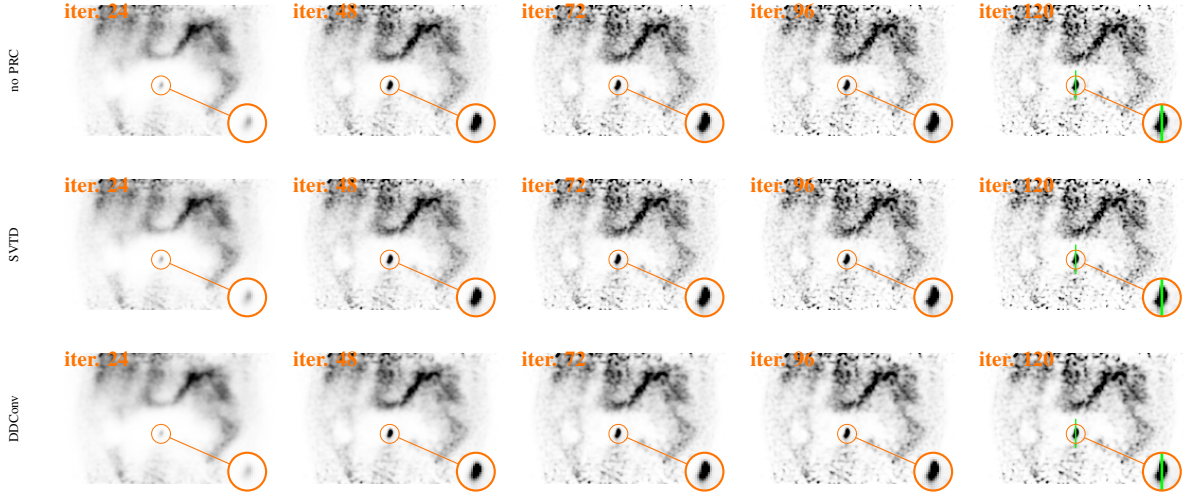


Fig. 8: Experiment 3—EM-reconstructed images (patient data) with no PRC, SVTD and DDCConv at different iterations.

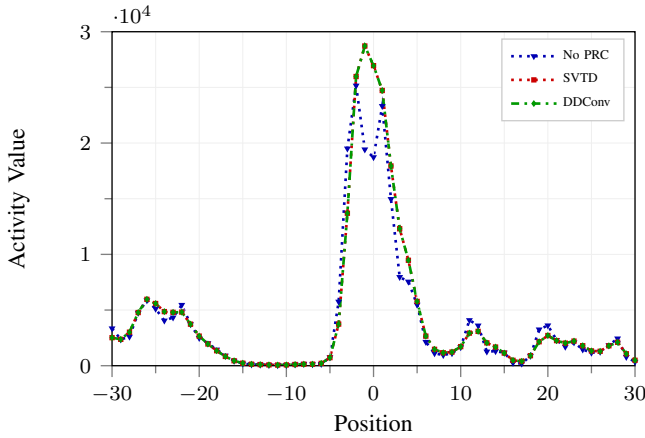


Fig. 9: Experiment 3—Line profiles of the reconstructed images (patient data, 120 EM iterations, cf. the green line in Figure 8) through the tumor with no PRC, SVTD and DDCConv.

The subset $\mathcal{S}_{\text{hom}}^l$ is the l th ‘homogeneous’ area, i.e., the area in material l on which an emitted positron is certain to annihilate with an electron in the same material. Conversely, the set

$$\mathcal{S}_{\text{het}} = \bigcap_{l=1}^L \overline{\mathcal{S}_{\text{hom}}^l} \quad (15)$$

is the ‘heterogeneous’ area.

B. Forward Operator

We first defined the *homogeneous* blurring operator $\mathbf{B}_{\text{hom}}(\boldsymbol{\mu})$, which is computed by separately convolving the entire activity image \mathbf{x} with the kernels \mathbf{h}_l and masking the resulting image by $1_{\mathcal{S}_{\text{hom}}^l}$ (the indicator function of $\mathcal{S}_{\text{hom}}^l$), then performing the sum

$$\mathbf{B}_{\text{hom}}(\boldsymbol{\mu}) \mathbf{x} = \sum_{l=1}^L \left(\mathbf{x} \odot 1_{\mathcal{S}_{\text{hom}}^l} \right) * \mathbf{h}_l, \quad (16)$$

where ‘ \odot ’ denotes the element-wise vector multiplication.

For voxels in the heterogeneous subset \mathcal{I} , a dynamic kernel is needed. At each voxel $j \in \mathcal{I}$, the PR predictor \mathbf{G}_{θ} is used to compute a local PSF w_j from its attenuation neighborhood $\boldsymbol{\mu}_{\mathcal{N}_j}$ and distance vector \mathbf{d} . The *heterogeneous* PR blurring operator $\mathbf{B}_{\text{het}}(\boldsymbol{\mu})$ is defined at each voxel k as

$$[\mathbf{B}_{\text{het}}(\boldsymbol{\mu}) \mathbf{x}]_k = \sum_{j \in \mathcal{N}_k \cap \mathcal{S}_{\text{het}}} w_{j \rightarrow k} \cdot x_j \quad (17)$$

which is computed by omitting voxels $j \notin \mathcal{S}_{\text{het}}$ in Algorithm 1.

Finally, we have

$$\mathbf{B}(\boldsymbol{\mu}) = \mathbf{B}_{\text{hom}}(\boldsymbol{\mu}) + \mathbf{B}_{\text{het}}(\boldsymbol{\mu}) \quad (18)$$

Backward Operator

The transposed homogeneous blurring operator $\mathbf{B}_{\text{hom}}(\boldsymbol{\mu})^{\top}$ is obtained by interchanging the multiplication with the indicator function $1_{\mathcal{S}_{\text{hom}}^l}$ and the convolution with the isotropic kernel \mathbf{h}_l , i.e.,

$$\mathbf{B}_{\text{hom}}(\boldsymbol{\mu})^{\top} \mathbf{z} = \sum_{l=1}^L (\mathbf{x} * \mathbf{h}_l) \odot 1_{\mathcal{S}_{\text{hom}}^l}, \quad (19)$$

while $[\mathbf{B}_{\text{het}}(\boldsymbol{\mu})^{\top}]$ is defined as

$$[\mathbf{B}(\boldsymbol{\mu})_{\text{het}}^{\top} \mathbf{z}]_j = \begin{cases} \sum_{k \in \mathcal{N}_j} w_{j \rightarrow k} \cdot z_k & \text{if } j \in \mathcal{S}_{\text{het}}, \\ 0 & \text{otherwise,} \end{cases} \quad (20)$$

which is computed by omitting voxels $j \notin \mathcal{S}_{\text{het}}$ in Algorithm 2.

Finally, we have

$$\mathbf{B}(\boldsymbol{\mu})^{\top} = \mathbf{B}_{\text{hom}}(\boldsymbol{\mu})^{\top} + \mathbf{B}_{\text{het}}(\boldsymbol{\mu})^{\top}. \quad (21)$$

ACKNOWLEDGMENT

All authors declare that they have no known conflicts of interest in terms of competing financial interests or personal relationships that could have an influence or are relevant to the work reported in this paper.

REFERENCES

- [1] P. Gavriilidis, M. Koole, S. Annunziata, F. M. Mottaghy, and R. Wierts, "Positron range corrections and denoising techniques for gallium-68 PET imaging: A literature review," *Diagnostics*, vol. 12, no. 10, p. 2335, 2022.
- [2] B. E. Hammer, N. L. Christensen, and B. G. Heil, "Use of a magnetic field to increase the spatial resolution of positron emission tomography," *Medical physics*, vol. 21, no. 12, pp. 1917–1920, 1994.
- [3] A. Wirrwar, H. Vosberg, H. Herzog, H. Halling, S. Weber, and H.-W. Muller-Gartner, "4.5 tesla magnetic field reduces range of high-energy positrons-potential implications for positron emission tomography," *IEEE Transactions on Nuclear Science*, vol. 44, no. 2, pp. 184–189, 1997.
- [4] S. E. Derenzo, "Mathematical removal of positron range blurring in high resolution tomography," *IEEE Transactions on Nuclear Science*, vol. 33, no. 1, pp. 565–569, 1986.
- [5] S. Haber, S. E. Derenzo, and D. Uber, "Application of mathematical removal of positron range blurring in positron emission tomography," *IEEE transactions on nuclear science*, vol. 37, no. 3, pp. 1293–1299, 1990.
- [6] J. L. Herraiz, A. Bembibre, and A. López-Montes, "Deep-learning based positron range correction of PET images," *Applied sciences*, vol. 11, no. 1, p. 266, 2020.
- [7] N. Encina-Baranda, J. Lopez-Rodriguez, A. Lopez-Montes, P. Ibañez, Y. Zheng, J. Cabello, J. Udias, M. Conti, and J. Herraiz, "Deep-prc: A positron range correction tool for preclinical and clinical PET/CT images," in *2024 IEEE Nuclear Science Symposium (NSS), Medical Imaging Conference (MIC) and Room Temperature Semiconductor Detector Conference (RTSD)*, IEEE, 2024, pp. 1–2.
- [8] H. Xie, L. Guo, A. Velo, Z. Liu, Q. Liu, X. Guo, B. Zhou, X. Chen, Y.-J. Tsai, T. Miao, *et al.*, "Noise-aware dynamic image denoising and positron range correction for rubidium-82 cardiac PET imaging via self-supervision," *Medical Image Analysis*, vol. 100, p. 103 391, 2025.
- [9] A. Autret, "Amélioration qualitative et quantitative de reconstruction TEP sur plate-forme graphique," Ph.D. dissertation, Télécom Bretagne; Université de Bretagne Occidentale, 2015.
- [10] Y. Mellak, K. Chatzipapas, A. Bousse, C. C.-L. Rest, D. Visvikis, and J. Bert, "Fast-track of F-18 positron paths simulations," *arXiv preprint arXiv:2403.06307*, 2024.
- [11] J. Cal-Gonzalez, M. Perez-Liva, J. L. Herraiz, J. J. Vaquero, M. Desco, and J. M. Udias, "Tissue-dependent and spatially-variant positron range correction in 3D PET," *IEEE transactions on medical imaging*, vol. 34, no. 11, pp. 2394–2403, 2015.
- [12] O. Bertolli, A. Eleftheriou, M. Cecchetti, N. Camarlinghi, N. Belcari, and C. Tsoumpas, "Pet iterative reconstruction incorporating an efficient positron range correction method," *Physica medica*, vol. 32, no. 2, pp. 323–330, 2016.
- [13] R. Kraus, G. Delso, and S. I. Ziegler, "Simulation study of tissue-specific positron range correction for the new biograph mMR whole-body PET/MR system," *IEEE transactions on nuclear science*, vol. 59, no. 5, pp. 1900–1909, 2012.
- [14] H. Kertész, T. Beyer, V. Panin, W. Jentzen, J. Cal-Gonzalez, A. Berger, L. Papp, P. L. Kench, D. Bharkhada, J. Cabello, *et al.*, "Implementation of a spatially-variant and tissue-dependent positron range correction for PET/CT imaging," *Frontiers in Physiology*, vol. 13, p. 818 463, 2022.
- [15] T. Merlin and D. Visvikis, "Deep learning approach for positron range correction in PET image reconstruction," in *2024 IEEE Nuclear Science Symposium (NSS), Medical Imaging Conference (MIC) and Room Temperature Semiconductor Detector Conference (RTSD)*, IEEE, 2024, pp. 1–1.
- [16] Y. Mellak, A. Bousse, T. Merlin, E. Emond, and D. Visvikis, "One linear layer is all you need for positron range estimation and correction," in *2024 IEEE Nuclear Science Symposium (NSS), Medical Imaging Conference (MIC) and Room Temperature Semiconductor Detector Conference (RTSD)*, IEEE, 2024, pp. 1–1.
- [17] S. Jan, G. Santin, D. Strul, *et al.*, "GATE: A simulation toolkit for PET and SPECT," *Physics in Medicine & Biology*, vol. 49, no. 19, p. 4543, 2004.
- [18] L. Shepp and Y. Vardi, "Maximum likelihood reconstruction for emission tomography," *IEEE transactions on medical imaging*, vol. 1, no. 2, pp. 113–122, 1982.
- [19] A. J. Reader, S. Ally, F. Bakatselos, R. Manavaki, R. J. Walledge, A. P. Jeavons, P. J. Julyan, S. Zhao, D. L. Hastings, and J. Zweit, "One-pass list-mode EM algorithm for high-resolution 3-D PET image reconstruction into large arrays," *IEEE Transactions on Nuclear Science*, vol. 49, no. 3, pp. 693–699, 2002.
- [20] J. Hu, B. Song, X. Xu, L. Shen, and J. A. Fessler, "Learning image priors through patch-based diffusion models for solving inverse problems," *arXiv preprint arXiv:2406.02462*, 2024.
- [21] A. Paszke, S. Gross, *et al.*, *Pytorch: An imperative style, high-performance deep learning library*, <https://pytorch.org/docs/stable/generated/torch.nn.ConvTranspose3d.html>, 2019.
- [22] M. D. Zeiler, D. Krishnan, G. W. Taylor, and R. Fergus, "Deconvolutional networks," in *2010 IEEE Computer Society Conference on computer vision and pattern recognition*, IEEE, 2010, pp. 2528–2535.
- [23] T. Merlin, S. Stute, D. Benoit, J. Bert, T. Carlier, C. Comtat, M. Filipovic, F. Lamare, and D. Visvikis, "CASToR: A generic data organization and processing code framework for multi-modal and multi-dimensional tomographic reconstruction," *Physics in Medicine & Biology*, vol. 63, no. 18, p. 185 005, 2018.
- [24] P. Tillet, H.-T. Kung, and D. Cox, "Triton: An intermediate language and compiler for tiled neural network computations," in *Proceedings of the 3rd ACM SIGPLAN International Workshop on Machine Learning and Programming Languages*, 2019, pp. 10–19.